water

MDPI

Article

Analysis of Unsteady Flow and Interstage Interference of Pressure Pulsation of Two-Stage Pump as Turbine Under Turbine Model

Yonggang Lu [1,2], Zhiwang Liu [2], Zequan Zhang [2], Weike Liao [1], Xiaolong Li [2] and Alexandre Presas [1,*]

[1] Centre de Diagnòstic Industrial i Fluidodinàmica, Universitat Politècnica de Catalunya, 08028 Barcelona, Spain; yonggang.lu@upc.edu (Y.L.); weike.liao@upc.edu (W.L.)
[2] School of Energy and Power Engineering, Jiangsu University, Zhenjiang 212013, China; 2212206013@stmail.ujs.edu.cn (Z.L.); 2222211082@stmail.ujs.edu.cn (Z.Z.); 2111911003@stmail.ujs.edu.cn (X.L.)
* Correspondence: alexandre.presas@upc.edu

Abstract: The process pump as turbine (PPAT) serves as a crucial component for recovering high-pressure energy from mediums used in chemical and refining processes. Ensuring the long-term safe and stable operation of PPAT in high-temperature and high-pressure environments is essential, with pressure pulsation being one of its most significant external characteristic indicators. This study investigates the evolution of vortex structure distribution and the generation and propagation mechanisms of pressure pulsation in a two-stage PPAT operating in turbine mode. Results indicate that the uniformity of the pressure coefficient (Cp) gradient distribution is poorer in the first stage runner compared to the second stage, with a larger distribution area of high-strength vortices. In the draft tube, vortex strength increases with rising flow rates, and the flow around the circular cylinder on one side gradually develops to both sides. In the two-stage diffusers, the primary source of pressure pulsation is the dynamic and static interference effect between the two impellers and the corresponding diffuser tongue. The interstage interference with a frequency of n*15fn is most pronounced in the inflow runner, gradually weakening along the flow direction, and ultimately disappearing in the draft tube. In addition, more low-frequency signals with a frequency of 0.5fn are captured in the draft tube under large flow conditions, which is mainly generated by the vortex band in the draft tube. The low-frequency pulsation energy is high and the attenuation is slow, which has a great destructive effect on the energy recovery system of the PPAT.

Keywords: pump as turbine; turbine mode; pressure pulsation; rotor–stator interaction; interstage interference

Citation: Lu, Y.; Liu, Z.; Zhang, Z.; Liao, W.; Li, X.; Presas, A. Analysis of Unsteady Flow and Interstage Interference of Pressure Pulsation of Two-Stage Pump as Turbine Under Turbine Model. *Water* **2024**, *16*, 3100. https://doi.org/10.3390/w16213100

Academic Editor: Giuseppe Pezzinga

Received: 7 September 2024
Revised: 22 October 2024
Accepted: 22 October 2024
Published: 29 October 2024

1. Introduction

The chemical process pump as turbine (PPAT) is a vital infrastructure component for recovering high-pressure energy from mediums used in chemical and refining processes [1,2]. When the impeller rotates forward, it functions as a pump, providing energy for the flow of media within the chemical refining system. Conversely, when the impeller rotates in reverse, it operates as a turbine, converting the system's high-pressure residual energy into electrical energy [3,4]. To ensure the safe operation of chemical process systems in high-temperature and high-pressure environments, the PPAT must exhibit high reliability and long-term stable performance [5]. Therefore, it is essential to conduct in-depth research on the internal flow mechanisms and operational stability of the PPAT and provide a theoretical basis for the optimal design and operation of the PPAT.

Many scholars have studied single-stage centrifugal [6–9] and axial-flow pumps as turbines [10–12], but there are few relevant studies on two-stage or multi-stage pumps as turbines. Massimiliano et al. [13] quantitatively analyze the energy conversion characteristics of the PAT, and propose a model based on analytical equations, where the

optimal efficiency point (BEP) of the PAT can be predicted. Derakhshan et al. [14] propose a procedure for selecting a suitable pump to work as a turbine in a small hydro-site. Zhang et al. [15] used numerical and experimental measurements to evaluate the unsteady flow in the PAT by analyzing the distribution of the pressure pulsations in the pump condition. Feng [16] conducted a numerical simulation on a multistage centrifugal pump, analyzed the unsteady characteristics of flow velocity, pressure and so on, and studied the mechanism of rotor–stator interference in the multistage pump. Wang et al. [17] obtained more reliable results by comparing different grid numbers, turbulence models, convergence accuracy, and surface roughness, using appropriate setting methods, and ensuring the integrity of the computational model. Yang et al. [18,19] used the CFD method to analyze the steady-state performance of PAT under different radial gaps and found that the dynamic static interference between the rotating impeller and the stationary volute can cause high-frequency unsteady pulsation inside the volute and low-frequency unsteady pressure pulsation inside the impeller. Li et al. [5] studied the impact of timing effects on the performance of PAT in the turbine condition and found that changing the sequence position of the two-stage runner can improve the hydraulic efficiency of the PAT. He [20] studied the hydraulic performance of the mixed-flow pump as turbine with forward curved blades with wrap angles of 20°, 35° and 50°, respectively. Bi et al. [21] studied the effects of the speed of the impeller and blade number of the diffuser on the hydraulic performance of PAT and found that the variation trend of the external characteristic curve of the turbine was basically the same at a different speed. Chen et al. [1] analyzed the effect of impeller blade inlet angle on pressure pulsation and the hydraulic efficiency of PAT in the turbine condition. Previous research has primarily focused on single-stage pumps as turbines (PATs), with relatively little attention given to multi-stage PATs [22] and the mutual influence and interference mechanisms between stages. And these studies mainly analyzed the influence of geometric parameters on the external characteristics of PAT.

This study addresses this gap by examining the internal flow mechanism and pressure pulsation characteristics of a two-stage PPAT operating in turbine mode. While many scholars have explored the transient flow characteristics of multi-stage pumps [23–25], there is limited understanding of the transient flow mechanisms in multi-stage PATs under turbine conditions. The hydraulic characteristics of a PAT working as a turbine are significantly different from those when it operates as a pump. This study analyzes the internal flow mechanism, pressure pulsation propagation, and phase superposition effects between the two-stage impellers under turbine conditions. These insights will enhance our understanding of PAT operational status and provide a theoretical foundation for optimizing PAT design.

2. Materials and Methods

2.1. Research Object

In this study, a two-stage PPAT was used as the research object. When the PPAT works as a pump, its design parameters are as follows: flow Q_p = 300 m^3/h, head Hp = 245 m, speed np = 2980 r/min. When it is working as the turbine, its rotational speed remains unchanged, but the direction of rotation is the opposite, that is, nt = −2980 r/min. Figure 1 shows the three-dimensional structure of the fluid domain of the PPAT. The PPAT is a two-stage structure; the first-stage impeller has 3 blades and the second-stage impeller has 5 blades. The two-stage diffuser adopts spiral double outlet volute and spiral single outlet volute, respectively. The main design parameters of the PPAT are shown in Table 1. From published studies [26], for two-stage PATs with high head, there will be strong interference between two impellers, especially the pressure pulsation characteristics under the turbine mode. Therefore, the pressure pulsation characteristics of the PPAT need to be analyzed to obtain the interference mechanism between the two-stage impellers. In this study, only the unsteady flow characteristics and the pressure pulsation characteristics of the PPAT in the turbine condition were studied.

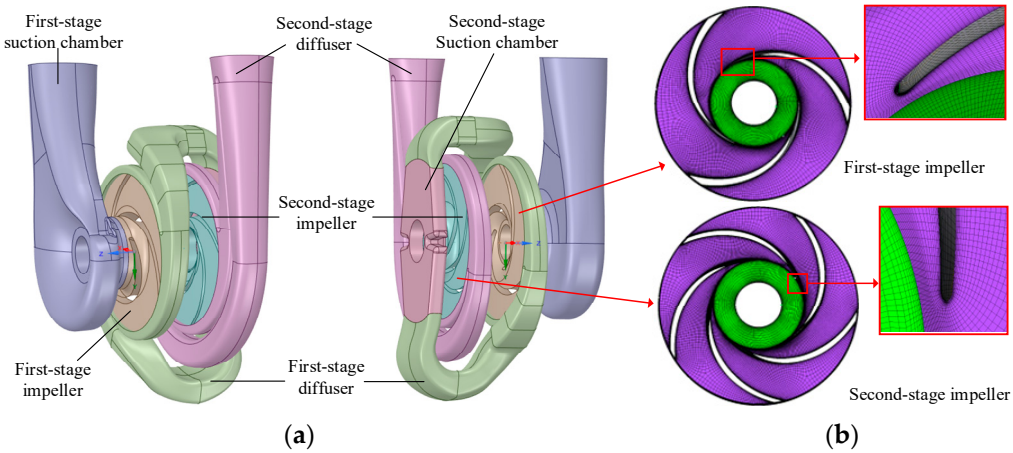

Figure 1. Fluid domain and mesh of the PPAT. (**a**) 3Dmodel of PAT; (**b**) Meshing of the impeller.

Table 1. Main parameters of the two-stage PPAT.

Impeller Parameters of First Stage	Value	Impeller Parameters of Second Stage	Value
Impeller inlet diameter, mm	158	Impeller inlet diameter, mm	140
Impeller hub diameter, mm	80	Impeller hub diameter, mm	95
Impeller outlet diameter, mm	348	Impeller outlet diameter, mm	348
Impeller outlet width, mm	22.5	Impeller outlet width, mm	17

2.2. Numerical Calculation Settings

In order to obtain the pressure pulsation signal in the PPAT, the unsteady numerical simulation method is used to monitor the pressure in the PPAT under the turbine condition. The setting of the monitoring points on the PPAT is shown in Figure 2. In the first-stage suction chamber, 6 monitoring points are arranged, P2–P7; in the first-stage diffuser, 3 monitoring points are arranged, P8–P10; in the second-stage suction chamber, 2 monitoring points are arranged, P11–P12; in the second-stage diffuser, 3 monitoring points are arranged, P13–P15. By capturing the pressure pulsation signal of the above 15 monitoring points, the unstable flow characteristics caused by the interference between the two-stage impellers can be analyzed.

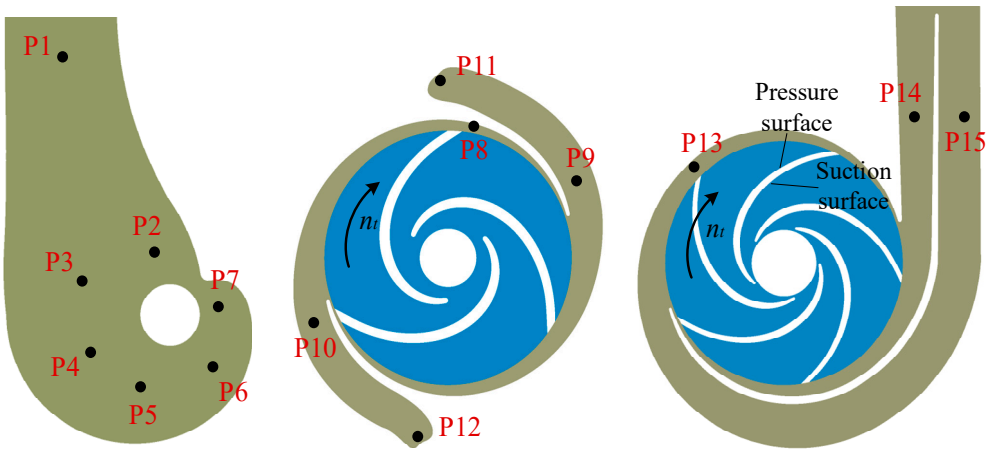

Figure 2. The monitoring point of the PPAT.

The software ANSYS CFX was used for CFD calculations, and the software ICEM 14.0 was used to generate meshes. The CFD setting is shown in Table 2. The SST k-ω turbulence model based the Eddy Viscosity Model was selected, and the dynamic–static interface surface was set as the Frozen Rotor interface; the boundary conditions of total pressure

inlet and static pressure outlet were set, respectively [27], and the rotation speed of the two impellers was set to 2980 r/min. The grid independence is verified by calculating the head and efficiency of the PPAT with different meshes under design condition. When the number of cells is more than 5.25 million, the change of the head and efficiency of the PPAT is less than 0.5% [26,28,29]. In order to ensure the accuracy and economy of the calculation, the refined near-wall grid scale was used in this study to ensure that the y+ value of the impeller can be kept within 200. In addition to the grid independence being checked, plan IV was selected and the total number of grids was determined to be 5.25 million, as shown in Table 3. In this study, the mesh of the impeller was hexahedral structure mesh, while other flow components use tetrahedral unstructured meshes. The mesh quality of all flow components was greater than 0.25. The total time for unsteady calculations is set to 10 rotation cycles, and every time step is set to $\Delta t = 60/2980/180 = 1.11857 \times 10^{-4}$ s. The last two cycles of the calculation results are used for analysis.

Table 2. Settings for numerical simulations.

Setting	Value/Type
Turbulence model	SST k-ω
Inlet boundary	Total pressure inlet, different pressure
Outlet boundary	Static pressure outlet, 10 kPa
Dynamic and static interface	Transient rotor stator
Initial condition	Steady calculation result

Table 3. Grid independence test under design condition.

	First-Stage Impeller		Second-Stage Impeller		PAT	
	Number	Maximum y+	Number	Maximum y+	Number	Head
Plan I	560,348	797	559,036	621	2,855,310	439.1
Plan II	763,289	570	760,424	502	3,686,331	445.7
Plan III	885,199	343	891,572	262	4,339,373	448.8
Plan IV	1,216,396	172	1,213,125	157	5,254,052	451.3
Plan V	1,548,656	96	1,564,722	83	6,513,677	451.5

2.3. Experimental Verification

In order to verify the accuracy of the numerical calculation, the operation data of the residual pressure power generation process of the PPAT are collected on site, as shown in Figure 3. The pressure transmitter is installed at the inlet and outlet of the PPAT to measure the pressure at the inlet and outlet, with a test accuracy of ±0.1%. An electromagnetic flowmeter is installed at the inlet pipeline to measure the real-time flow of the PPAT, with a test accuracy of ±0.5%. The real-time output power of the PPAT is collected by the generator. The signals of the flowmeter, pressure transmitter, and generator were input to the computer through the EST2008 measurement system to calculate the head, output power and efficiency of the PPAT. The inlet energy is adjusted by adjusting the inlet valve, and the hydraulic performances of the PPAT at different operating conditions are obtained [28,30,31]. Figure 4 shows the comparison between the test and CFD of PPAT, which shows that the head deviation is less than 5% and the efficiency deviation is less than 3%, indicating that the numerical calculation is accurate.

Figure 3. Experimental site of residual pressure power generation.

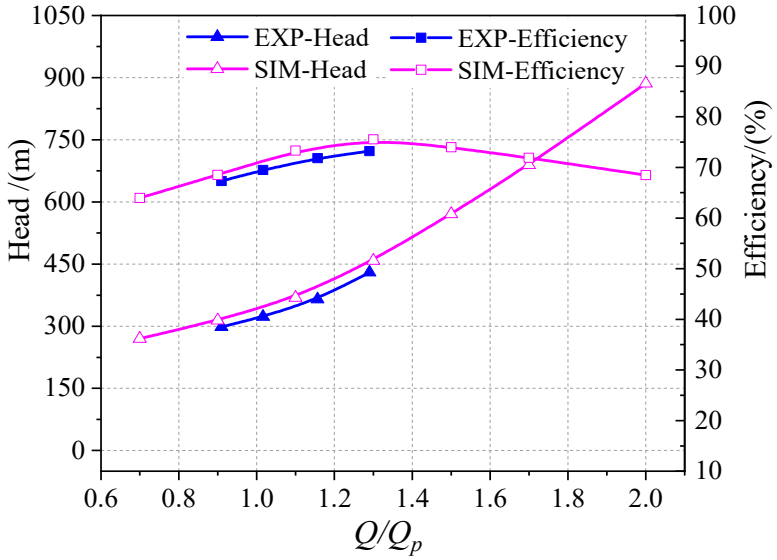

Figure 4. Hydraulic characteristic curve of the PPAT in turbine mode.

3. Results and Discussion

3.1. The Performance of the Model PPAT

Figure 4 shows the performance curve of the PPAT and the comparison with the experiment. From the efficiency curve, the highest efficiency under the turbine condition occurs at $1.3Q_p$ (Q_p is the design flow of its pump condition). The efficiency zone is between $1.0Q_p$ and $1.7Q_p$, with an efficiency range of 71.5%~76.1%. From the head curve, the head of the PPAT gradually increases with the flow rate and is proportional to the square of the flow as a whole. Compared with the pump mode, the flow ratio Qt/Q_p and the head ratio Ht/Hp under the optimal working conditions in turbine mode are 1.44 and 1.64, respectively (Qt is the flow of turbine; Ht is the head of turbine). This indicates that the increase in flow rate of PPAT during the turbine mode has a greater impact on the variation of head. Pressure pulsation is actually a representation of head fluctuation. Since the head range of the PPAT is 300~900 m, the hydraulic excitation force generated by the small head fluctuation will also be a large value. Therefore, pressure pulsation is a very important indicator for the safe operation of the PPAT.

3.2. Analysis of Internal Flow Structure of the PPAT

The dimensionless parameter C_p was used to analyze the pressure distribution in the middle section of the impeller. The definition is shown in the following formula.

$$C_p = \frac{P - \overline{P}}{0.5\rho u^2} \quad (1)$$

where P is the local pressure inside the section; $\overline{P}$ is the average pressure of the section; ρ is the density of medium; u is the circumferential velocity at the impeller outlet.

Figures 5–7 show the distribution of C_p in the impeller, diffuser and the suction chamber of each stage under different conditions. From Figure 5, the pressure gradually decreases along the flow direction and reaches the minimum at the inlet of the impeller (Figure 5b), and there is a local low-pressure zone (A-zone) near the suction side at the inlet of the impeller. From the C_p distribution of each cross-section, the corresponding $\nabla C_p (\nabla C_p = C_{p_{max}} - C_{p_{min}})$ values under $0.9Q_p$, $1.3Q_p$ and $2.0Q_p$ conditions are 1.22, 1.56 and 3.37, respectively. According to the gradient distribution of C_p, the pressure changes inside the impeller under the $1.3Q_p$ flow condition are the most uniform, the pressure gradient distribution under the $2.0Q_p$ flow condition is the worst, and the C_p value gradually increases from the suction side to the pressure side. It can also be found that there was a local low-pressure zone (B-zone, Figure 5c) in the middle of the flow channel under the $2.0Q_p$ condition, representing the fact that there was a vortex area in the impeller flow channel.

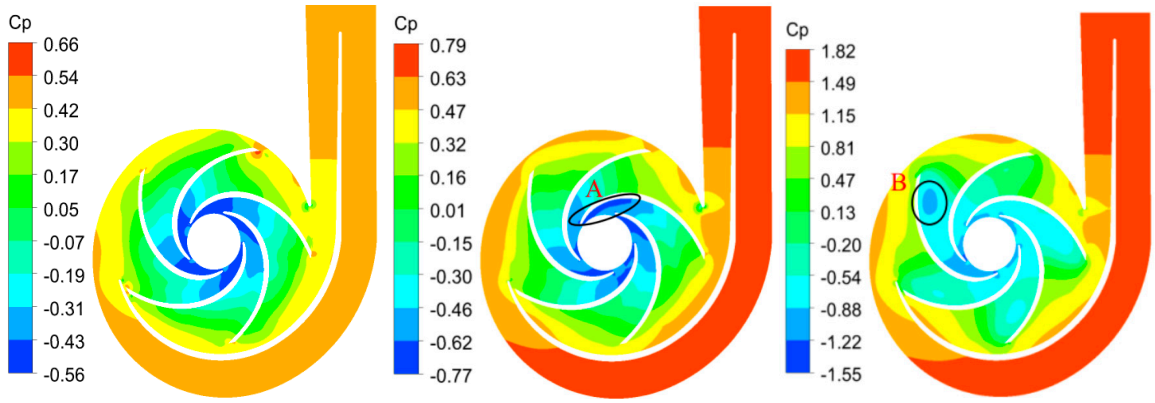

(**a**) $0.9Q_p$ (**b**) $1.3Q_p$ (**c**) $2.0Q_p$

Figure 5. Pressure coefficient distribution of the section where the second-stage impeller is located.

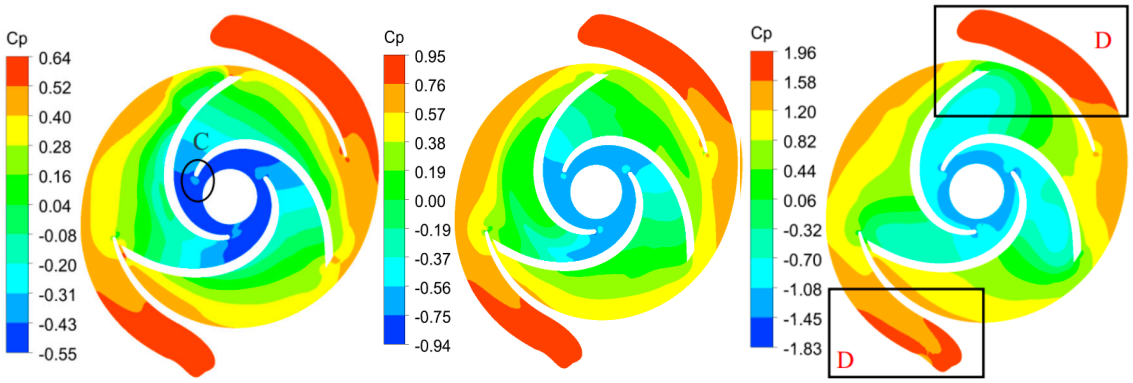

(**a**) $0.9Q_p$ (**b**) $1.3Q_p$ (**c**) $2.0Q_p$

Figure 6. Pressure coefficient distribution of the section where the first-stage impeller is located.

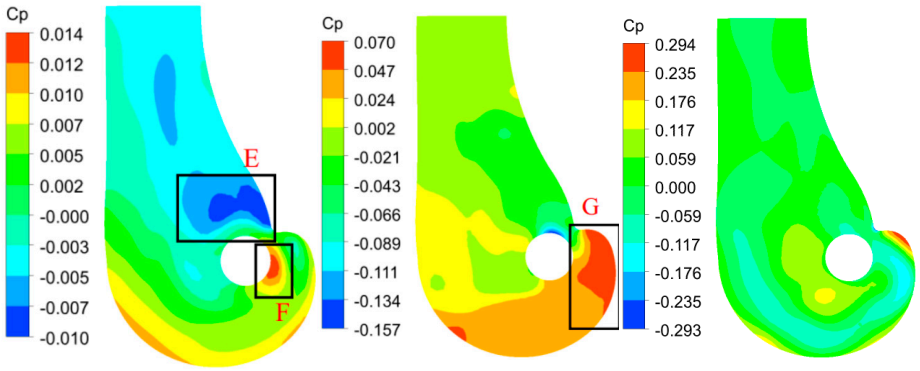

(**a**) $0.9Q_p$ (**b**) $1.3Q_p$ (**c**) $2.0Q_p$

Figure 7. Pressure coefficient distribution of the section where the first-stage suction chamber is located.

From Figure 6, the C_p distribution in the first-stage impeller shows lack of uniformity, especially at the rotor–stator interaction between the impeller outlet and the diffuser; the C_p distribution presents a sawtooth shape. This is mainly due to the pressure change behind the pressure surface caused by the impeller rotating blade sweeping over the diffuser tongue. There is a high-pressure zone (C-zone, Figure 6a) near the inlet of the impeller blade, where the pressure pulsation with the frequency of the blade frequency will be generated. From the C_p distribution of each section, the corresponding ∇C_p under $0.9Q_p$, $1.3Q_p$ and $2.0Q_p$ conditions is 1.19, 1.89 and 3.79, respectively. The pressure changes inside the impeller are the most uniform under the $1.3Q_p$ condition, and the pressure gradient distribution is less uniform under the $2.0Q_p$ condition. From the C_p distribution of the diffuser, the pressure in the diffusion section of the diffuser shows obvious asymmetry, especially in the high-flow condition (D-zone, Figure 6c). It can also be found that high and low pressures are distributed on both sides of the tongue, and this phenomenon is more obvious with the flow rate increases.

In the turbine mode, the first-stage suction chamber is used as a draft tube. From Figure 7, under low-flow conditions, there are obvious high-pressure and low-pressure zones (E-zone and F-zone, Figure 7a) on both sides of the vortex tongue of the draft tube, which should be caused by the flow around the cylinder occurring on one side of the central circle of the draft tube. As the flow increases, the distribution of high and low pressures on both sides of the vortex tongue gradually disappears, and it may be that the flow around circular cylinder from one side develops into flow on both sides. Under the $0.9Q_p$ condition, the gradient change in C_p generally decreases along the flow direction, and this gradient change law gradually weakens with the flow rate increase. When the flow rate of PPAT reaches $2.0Q_p$, the cloud atlas of the whole cross-section shows an uneven distribution of local high and low pressures. It can also be found that the ∇C_p change in draft tube is significantly smaller than the cross-section where the impeller is located, and ∇C_p is only 0.587 when the flow rate reaches 2.0Qp.

Figures 8–10 show the vortex strength distribution of the water-passing components under different flow conditions, respectively. From Figure 8, on the section where the second-stage impeller is located, the large vortex is mainly distributed in the impeller channel. Under the conditions of $0.9Q_p$ and $1.3Q_p$, it is unevenly distributed in the five channels of the impeller, and the large vortex fills the entire flow channel of the impeller. The vortex strength of the impeller flow channel near the diffusion region of the diffuser (H-zone, Figure 8a) is significantly greater than that of the impeller channel far away from the diffusion region (I-zone, Figure 8a). This is primarily attributed to the fluid entering the H-zone first before proceeding into the I-zone, and the extended diffusion section within the I-zone effectively directs the flow within the flow field. Under the $2.0Q_p$ condition, the large vortex in the impeller channel mainly appears in the trailing edge of the blade and its

wake region develops near the suction surface of the blade, which is mainly caused by the flow separation.

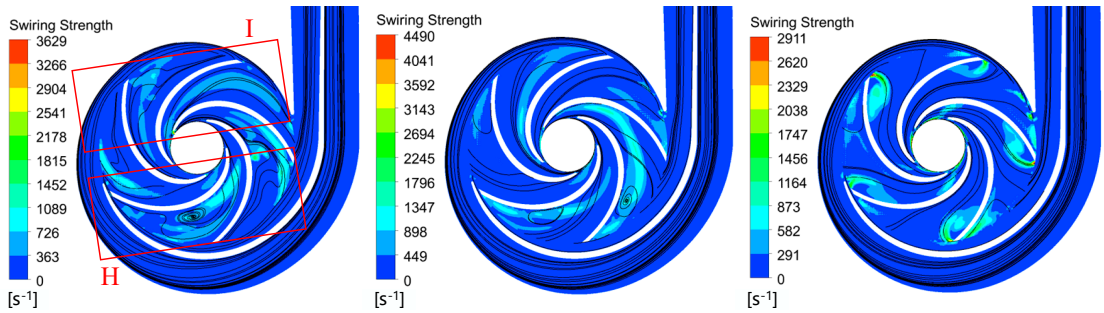

(**a**) 0.9Q_p (**b**) 1.3Q_p (**c**) 2.0Q_p

Figure 8. Vortex strength distribution of the section where the second-stage impeller is located.

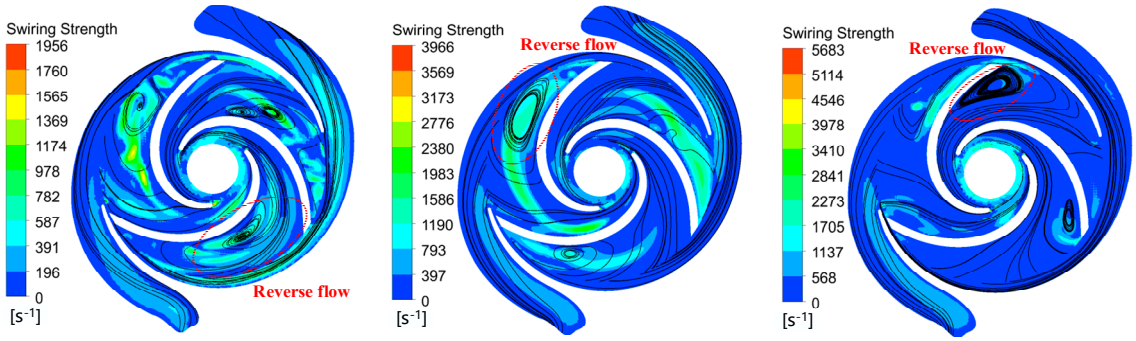

(**a**) 0.9Q_p (**b**) 1.3Q_p (**c**) 2.0Q_p

Figure 9. Vortex strength distribution of the section where the first-stage impeller is located.

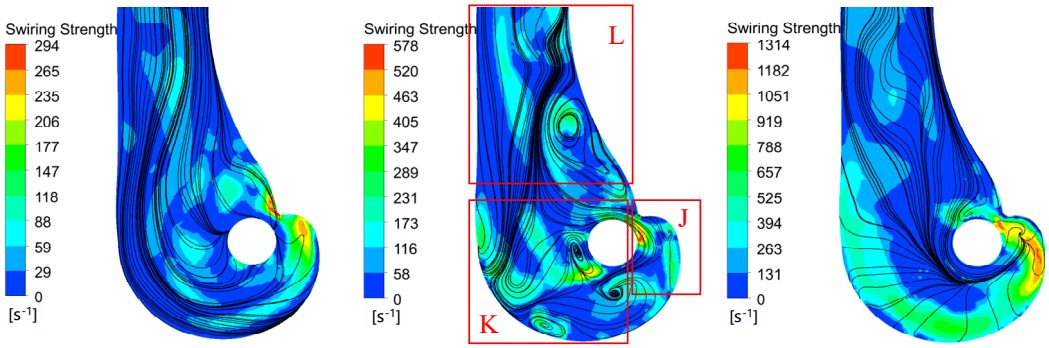

(**a**) 0.9Q_p (**b**) 1.3Q_p (**c**) 2.0Q_p

Figure 10. Vortex strength distribution of the section where the draft tube is located.

From Figure 9, the vortex distribution law of the section where the first-stage impeller is located is similar to that of the second stage as a whole, and the vortex distribution develops from filling the entire channel to a local high-intensity vortex within the impeller. However, the distribution area of the high-intensity vortex on the first stage section is larger. This is mainly due to the number of blades of the first-stage impeller being smaller, and there is greater speed slip in the channel, which also means that the pressure pulsation generated by the first-stage impeller may be stronger [32–34]. It can also be seen that large-scale vortices caused by reverse flow are formed in the impeller channel when the operating condition (0.9Q_p and 2.0Q_p) deviates from the optimal condition, and the scale of some vortices almost blocks half of the area of a single channel, but not all channels of the impeller are blocked.

In order to better analyze the vortex distribution in the draft tube (first-stage suction chamber), the draft tube is divided into three regions, J-Zone, K-Zone and L-Zone, as shown in Figure 10. From Figure 10, the vortex strength in the draft tube increases with the increase in flow, and the distribution area of the high-intensity vortex gradually extends from the tongue position (J-zone) to the downstream K-Zone and L-Zone along the outer spiral line. In low-flow conditions, after the fluid passes through the high-speed rotating impeller, the water flow on the draft tube is far from the central axis. With the increase in flow, the vortex band phenomenon of the draft tube is generated, and the inertial impact of fluid here (streamline) will also be large, which will increase the low-frequency pressure pulsation inside the PPAT. Under the $1.3Q_p$ condition, the flow pattern in the K-zone is disordered, and a large number of backflows and disorderly vortices appear, which is caused by the displacement of the water flow by the vortex band, and an obvious high-speed area appeared between the vortex band and the wall. With the increase in the flow rate, the high-strength vortex gradually transfers to the outer wall in the $2.0Q_p$ condition, and it can be seen from the streamline of the K and L-Zone that the direction of fluid flow is close to perpendicular to the outer wall of the draft tube, and the fluid has directly impacted the wall, which will cause strong noise and pressure pulsation.

3.3. Pressure Pulsations in the First-Stage Diffuser and Second-Stage Diffuser

In order to more specifically express the fluctuation of transient pressure within the PPAT and use the pressure pulsation amplitude to represent its periodic transient results [35,36], the expression of the pressure amplitude ΔP is:

$$\Delta P = P - \frac{1}{n} \cdot \sum_{i=1}^{n} P_i \tag{2}$$

where ΔP is the difference between the monitoring pressure and the average pressure of one cycle, Pa; *Pi* is the transient pressure value of monitoring point, Pa.

Figures 11 and 12 show the time domain diagram of pressure pulsation on the section where the impeller is located under different flow conditions. Under turbine mode, the second-stage diffuser is used as the inflow runner. Figure 13 shows the comparison of the maximum amplitude for one cycle ($\Delta P_{max} - \Delta P_{min}$) of the monitoring points under the condition of $0.9Q_p$, $1.3Q_p$ and $2.0Q_p$. From Figure 11, the pressure pulsations of P13 are significantly higher than at the other two monitoring points, which is most obvious when deviating from the optimal flow conditions. At the $0.9Q_p$ condition, the pressure curve of P13 has 11 peaks in one rotation period, including four large peaks and seven small peaks, of which the two small peaks at 0.8T are caused by the superposition of the peaks and valleys of the two different pressure waves. The pressure fluctuation pattern of P13 in the 0.6~1.0T cycle is completely different from the pressure pulsation in the first 1/2 cycle. It shows that the 0.6~1.0T is affected by the pressure fluctuations caused by the other impeller. By comparing the peak wave, we can determine that the superposition of the pressure fluctuations produced by other impeller occurs at this monitoring point. At the $1.3Q_p$ condition, the pressure change curve of P13 has fifteen peaks in one rotation period, including five large peaks and ten small peaks, which indicates that the pressure wave generated by the first stage impeller (three blades) propagates upstream and interferes with the second-stage impeller. Because the blade number of the first-stage impeller is 5 and the blade number of the second stage is 3, the fifteen amplitude troughs are mainly caused by the interference between the first-stage and the second-stage blades, but the five large peak troughs are caused because the monitoring point is closer to the impeller of the five blades. At the $2.0Q_p$ condition, the pressure change curve of P13 has five obvious peaks, indicating that the interference effect of the first-stage impeller is weak. From the above analysis, it can be seen that under optimal conditions, the pressure pulsation in the second-stage diffuser is influenced by the joint influence of the first-stage impeller and the second stage impeller, and when it deviates from the optimal conditions, it is mainly affected by the rotor–stator interaction between the second-stage impeller and the tongue

of the second-stage diffuser. From Figure 12, the pressure pulsation of P8, which is closer to the impeller outlet, is significantly stronger than that of P9 and P11 on the diffusion section. Under low-flow conditions, the pressure pulsation curves of P8–P11 are very disordered, but with the increase in flow, the regularity of pressure pulsation becomes stronger. And the peaks of the P8–P11 pressure curves are irregular sawtooth, which is mainly influenced by the upstream pressure wave. From Figure 13, the maximum amplitude of the monitoring points P8–P9 ($\Delta P_{max} - \Delta P_{min}$) increases with the increase in the flow, while the maximum amplitude of the monitoring points P11–P15 at the $1.3Q_p$ condition is significantly lower than that of $0.9Q_p$ and $2.0Q_p$. The monitoring points P14 and P15 are located far away from the impeller, and their amplitudes are significantly lower than those of other monitoring points. Therefore, the dynamic and static interference between the impeller and the diffuser tongue is the main reason for the strong pressure pulsation.

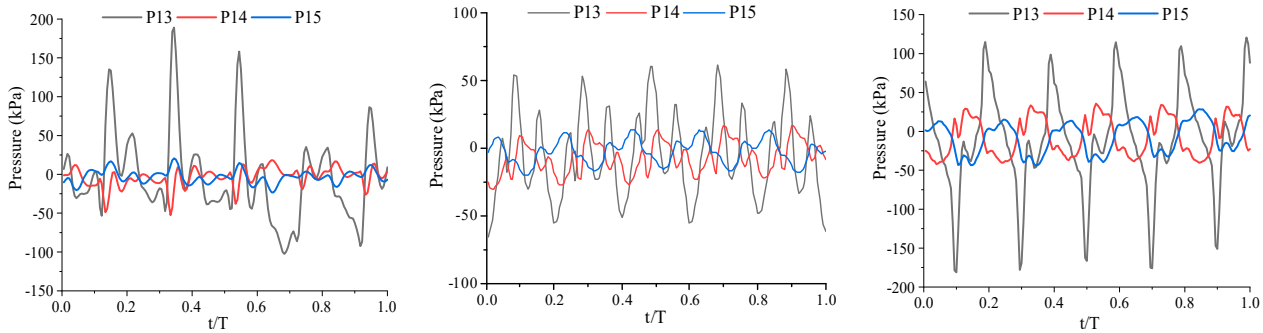

(**a**) $0.9Q_p$ (**b**) $1.3Q_p$ (**c**) $2.0Q_p$

Figure 11. Time domain diagram of pressure pulsation of monitoring points P13–P15.

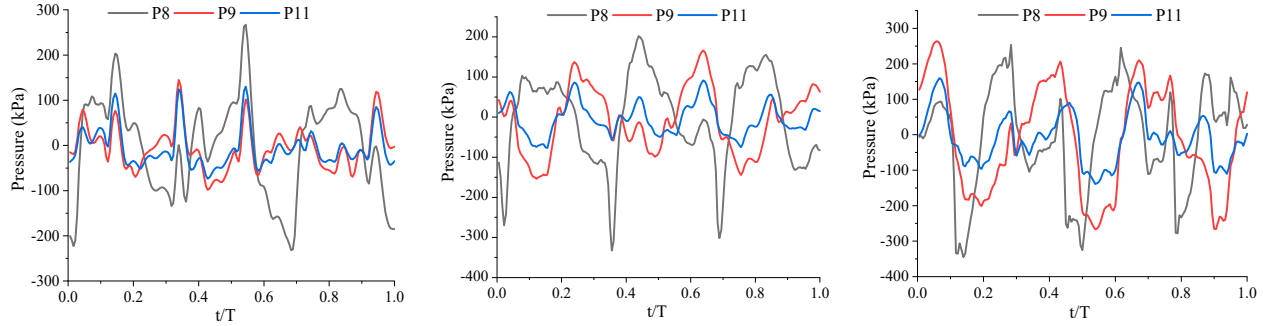

(**a**) $0.9Q_p$ (**b**) $1.3Q_p$ (**c**) $2.0Q_p$

Figure 12. Time domain diagram of pressure pulsation of monitoring points P8–P11.

In order to analyze the main factors causing pressure pulsation in PPAT and obtain the frequency spectrum characteristics of pressure pulsation, the time domain signal of pressure pulsation is subjected to FFT (fast Fourier transform) transformation, and the frequency spectrum of the monitoring points P8–P15 is obtained, as shown in Figures 14–16. From Figure 14, under the $0.9Q_p$ condition, the dominant frequency of monitoring points P11–P15 is the blade passing frequency fBPF2 (5fn) of the second-stage impeller, and the harmonic frequencies of 2 fBPF2, 3 fBPF2, 4 fBPF2 and 5 fBPF2 can also be monitored. The blade passing frequency is the most significant excitation frequency in rotating machinery. In the low-frequency band, the significant components of 0.5fn and fn are also observed. The dominant frequency of monitoring points P8–P9 is the blade passing frequency fBPF1 (3fn) caused by the first-stage rotor–stator interaction, but there are a large number of n*5f_n (n = 1, 2, 3. . .) in the frequency spectrum, indicating that there is pressure pulsation generated by the upstream impeller. From Figure 15, under the $1.3Q_p$ condition, the dominant frequency of the monitoring points P11–P15 are the blade frequency of the second-stage impeller and its multiplier, and the significant components of 0.5fn are also

observed in the low-frequency band. The dominant frequency of the monitoring point P8–P9 is the blade frequency fBPF1 of the first-stage impeller, and the amplitude generated is 2–5 times that of the other monitoring points. From Figure 16, under the 2.0Q_p condition, the dominant frequency of the monitoring point P8–P9 is the blade frequency fBPF1 of the first-stage impeller, and the dominant frequency of the monitoring points P11–P15 is the blade frequency fBPF2 of the second-stage impeller. It can be found that with the increase in flow, the harmonic component of the pressure pulsation gradually decreases, and the low-frequency components of 0.5fn are more easily captured. Meanwhile, with the increase in flow, the pressure pulsation amplitude of each monitoring point gradually increases, and the pressure pulsation amplitude of each monitoring point is shown as P8 > P9 > P11 ≈ P13 > P14 ≈ P15. The decrease in pressure pulsation amplitude along the flow direction indicates that the pressure wave is propagating upstream and there is no superposition of pressure waves.

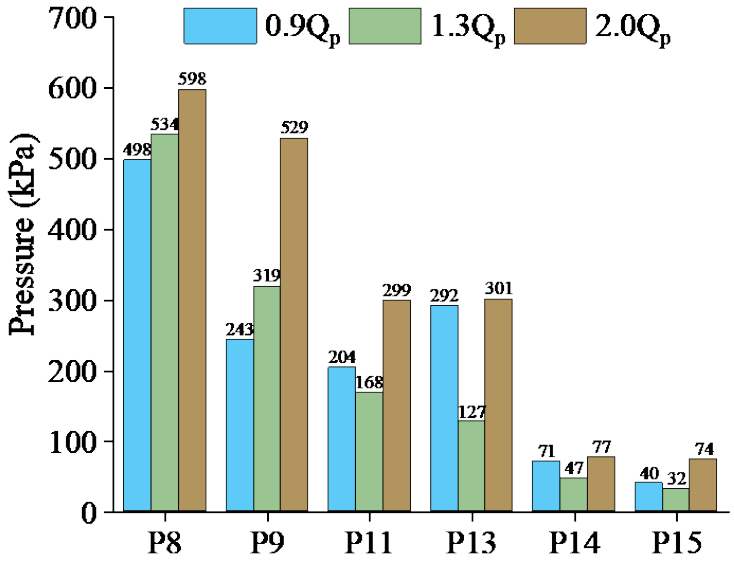

Figure 13. Comparison of the maximum amplitude of P8–P15 under different flow conditions.

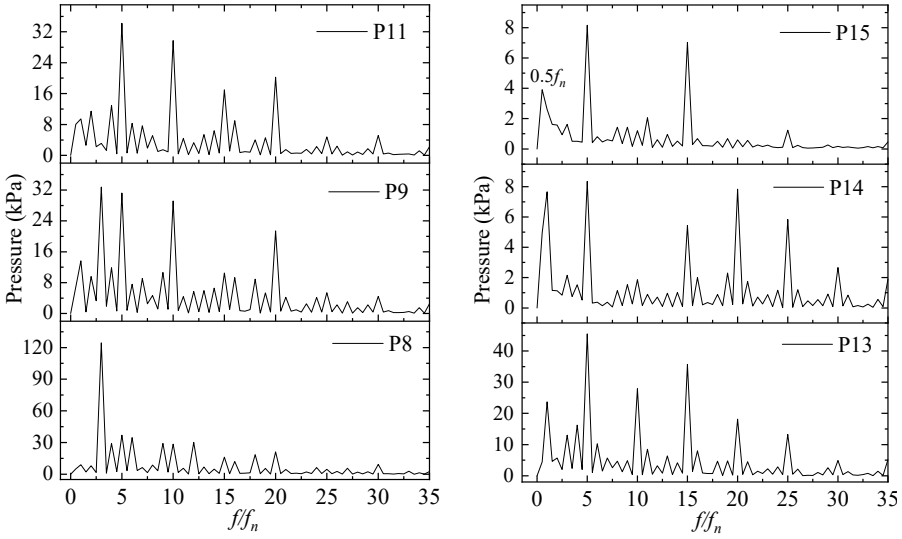

Figure 14. Frequency domain diagram of monitoring points P8, P9, P11, P13, P14, P15 under 0.9Q_p condition.

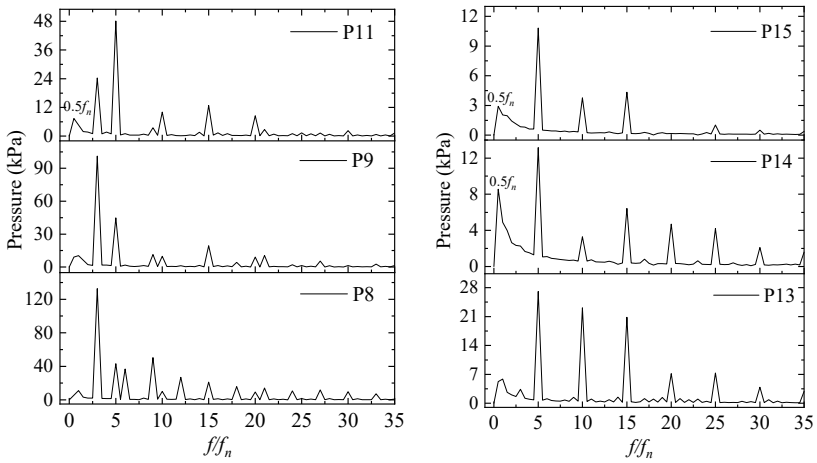

Figure 15. Frequency domain diagram of monitoring points P8, P9, P11, P13, P14, P15 under 1.3Q_p condition.

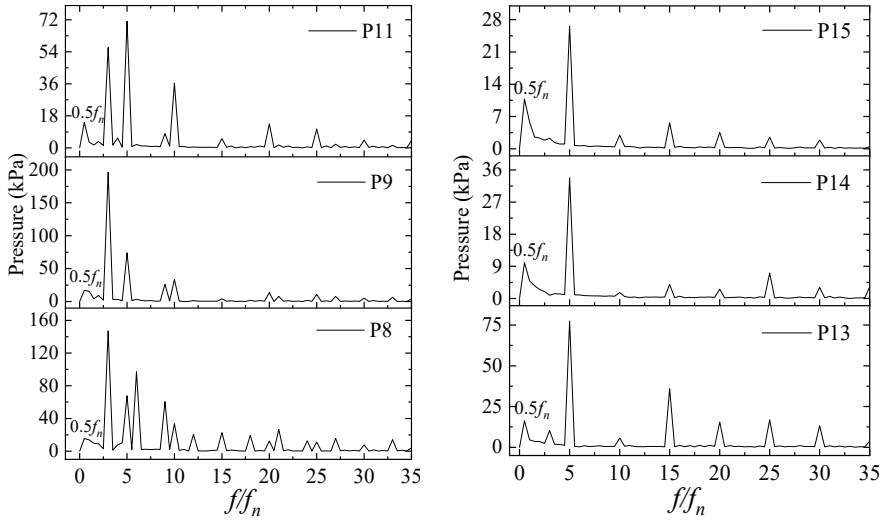

Figure 16. Frequency domain diagram of monitoring points P8, P9, P11, P13, P14, P15 under 2.0Q_p condition.

3.4. Pressure Pulsations in the Draft Tube

Figure 17 shows the time domain diagram of pressure pulsation in the first-stage suction chamber of the PPAT under different flow conditions. Under the turbine mode, the first-stage suction chamber is used as the draft tube. Figure 18 shows the comparison of the maximum amplitudes of the monitoring points within one rotation cycle under the conditions of 0.9Q_p, 1.3Q_p and 2.0Q_p. From Figure 17, the pressure curves of the monitoring points P1–P7 at the 0.9Q_p condition are close to overlapping, but as the flow increases, the pressure curves of P1–P7 gradually separate. Combined with Figure 10, it can be seen that as the flow rate increases, the flow state and vortex distribution in the tailpipe undergo significant changes, which is the main reason for the separation of the monitoring line. Under the conditions of 0.9Q_p and 1.3Q_p, the pressure curves of monitoring points P1–P7 in one rotation cycle show irregular fluctuation laws, which may be due to a large value of flow separation and reverse flow under low-flow conditions. Under the 2.0Q_p condition, the pressure curve of P1–P7 gradually showed a periodic fluctuation law, including five peaks and troughs in one rotation cycle. From Figure 18, the maximum amplitudes ($\Delta P_{max} - \Delta P_{min}$) of each monitoring point are basically the same. The maximum amplitude under the 2.0Q_p condition is twice that of the 1.3Q_p condition, which is mainly caused by the large angle of attack when the fluid enters the impeller when the operating conditions deviate from the optimal condition.

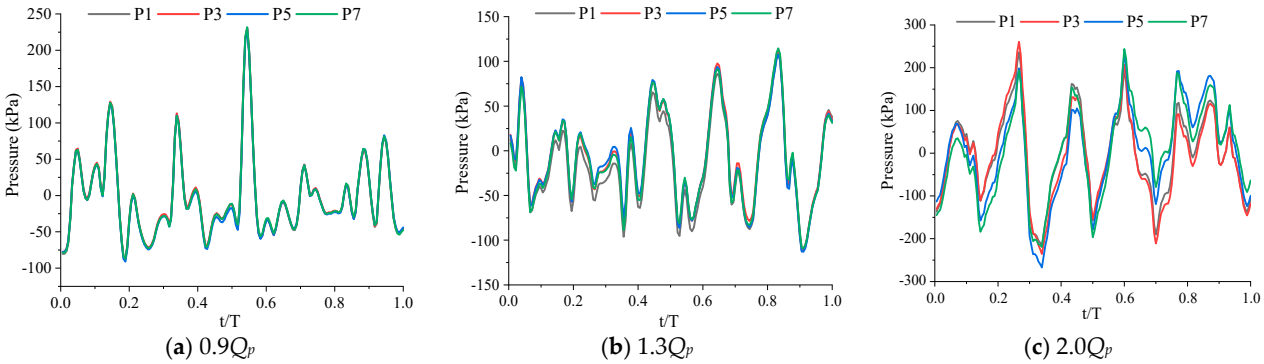

(**a**) 0.9Q_p (**b**) 1.3Q_p (**c**) 2.0Q_p

Figure 17. Time domain diagram of pressure pulsation of monitoring points P1–P7.

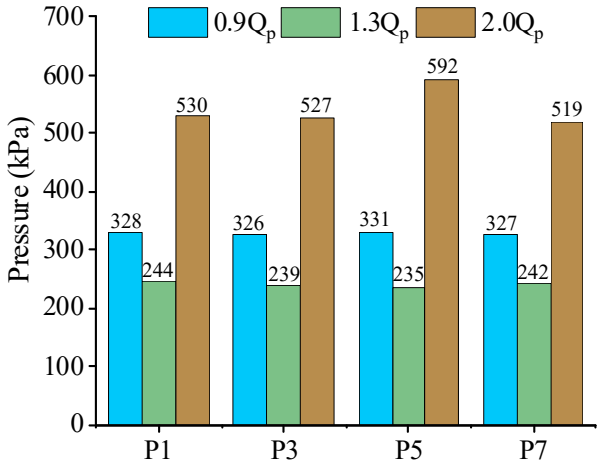

Figure 18. Comparison of the maximum amplitude of P1–P7 under different flow conditions.

Figures 19–21 show the pressure pulsation frequency domain diagrams of monitoring points P1–P7 under different flow conditions. From Figure 19, under the 0.9Q_p condition, the dominant frequency of the monitoring points P1–P7 is the blade frequency fBPF2 of the second-stage impeller. Meanwhile, there are a large number of pressure pulsations with a frequency of n*fn (n = 1, 2, 3…) in its spectrum, indicating that the rotational frequency fn is also the main factor affecting its pressure pulsation. From Figure 20, under the 1.3Q_p condition, the dominant frequency of the monitoring points P1–P7 are 5*fn (f_{BPF2}) and 6*fn (2* f_{BPF1}), indicating that the blade passing frequency of the first-stage impeller and the second-stage impeller are both the main factor that produces pressure pulsation. In the low-frequency band, the significant components of 0.5*fn are captured, and the corresponding amplitude increases with distance from the impeller, which is likely to be caused by the vortex band in the draft tube. Under the 2.0Q_p condition, the dominant frequency of the monitoring points P1–P7 is 6*fn (2* f_{BPF1}), and the other sub-frequencies that affect pressure pulsations are 5*fn, 3*fn, and 0.5*fn in turn. Combining Figures 19–21, it can be found that with the increase in flow, the pressure pulsation amplitude of P1–P7 gradually increases, and the maximum pulsation amplitude at the condition of 2.0Q_p is twice that of 0.9Q_p and 1.3Q_p. In addition, under different flow conditions, there are a large number of large-amplitude harmonic signals with a frequency of n*fn in the pulsation spectrum of the draft tube. With the increase in flow, the relative amplitude of the harmonic signal gradually decreases, which also explains the irregular fluctuation of pressure curves in Figure 17.

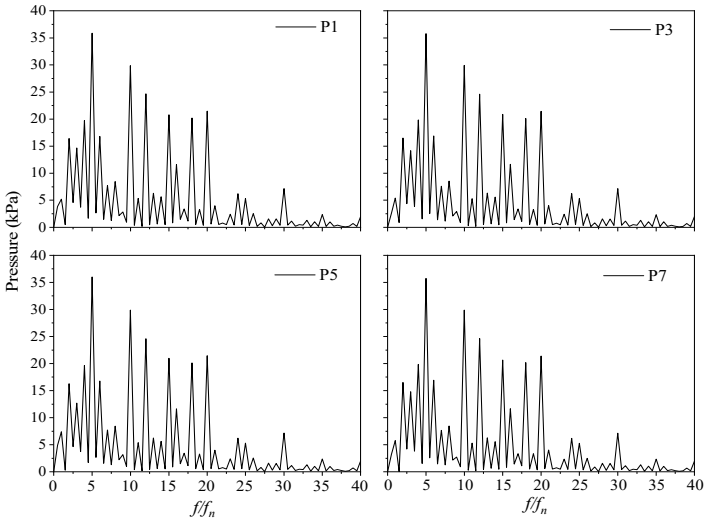

Figure 19. Frequency domain diagram of monitoring points P1, P3, P5, P7 under $0.9Q_p$ condition.

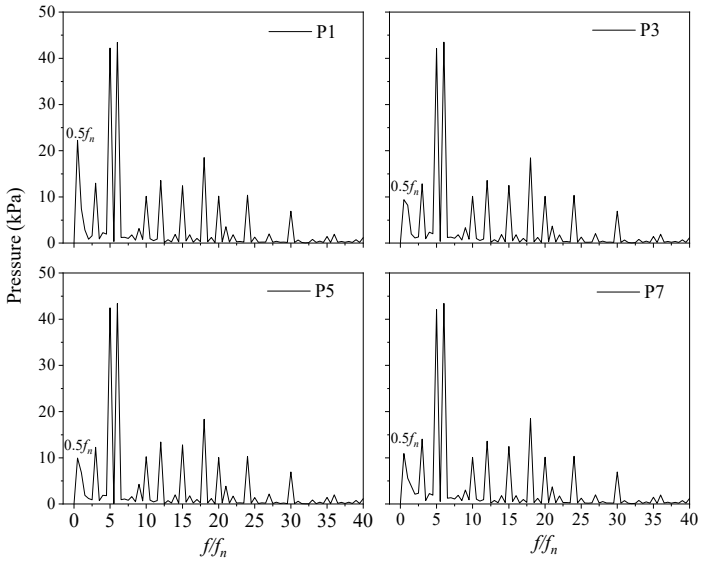

Figure 20. Frequency domain diagram of monitoring points P1, P3, P5, P7 under $1.3Q_p$ condition.

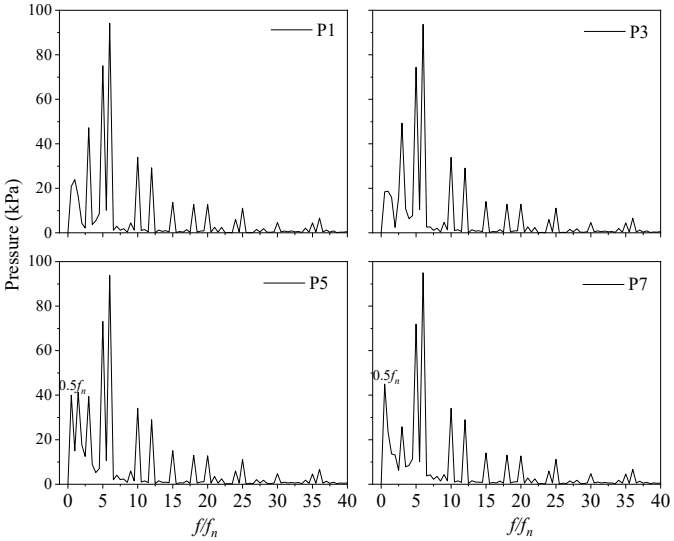

Figure 21. Frequency domain diagram of monitoring points P1, P3, P5, P7 under $2.0Q_p$ condition.

3.5. Analysis of Interstage Interference Between Two-Stage Impellers

Through the above analysis, it can be seen that there is obvious interstage interference between the two-stage impellers. Figure 22 shows the main frequency distribution of monitoring points P8–P15 under the conditions of $0.7Q_p$, $1.0Q_p$ and $1.3Q_p$. Figure 23 shows the amplitude distribution of the corresponding frequencies. From Figure 22, before the fluid enters the impeller (P13–P15), the main frequencies of the pressure pulsation are distributed at 5fn, the second-order frequency distribution at 0.5fn (4 times), 3fn (2 times), 10fn (1 time), 15fn (4 times) and 20fn (1 time), the third-order frequency is distributed at 0.5fn (3 times), 10fn (2 times), 15fn (3 times) and 20fn (1 time), and the fourth-order frequency is distributed at 0.5fn (2 times), 15fn (1 time), 20fn (2 times), and 25fn (4 times). It can be seen that before the fluid enters the impeller, the main factor affecting the pressure pulsation in the second-stage diffuser is the rotor–stator interaction between the second-stage impeller and the tongue of the second-stage diffuser. The interstage interference frequency n*15fn between the two-stage impellers appears 4 times in the statistics of the second-order frequency and 3 times in the statistics of the third-order frequency.

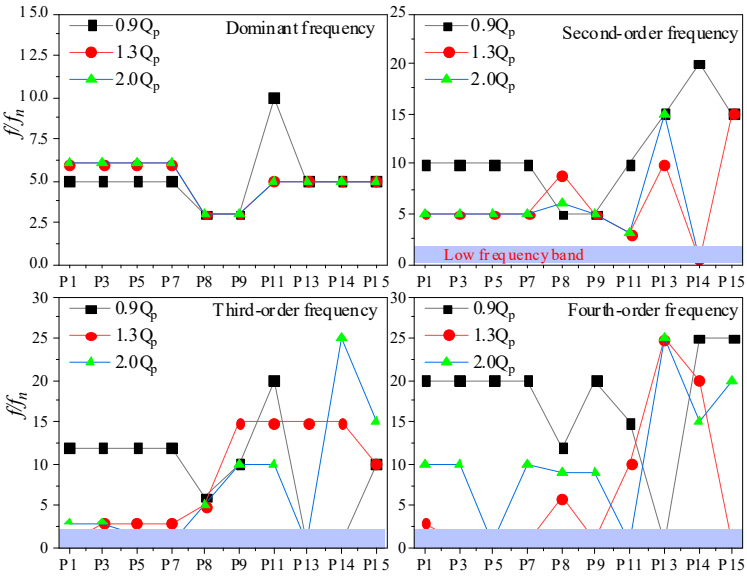

Figure 22. Distribution of main frequency, second-order, third-order and fourth-order frequency of the monitoring points.

Combined with Figure 23, the amplitude of the second-order and third-order frequency exceeds 50% of the amplitude of the main frequency, so the interstage interference between the two-stage impellers has already produced a strong pressure pulsation in the second-stage diffuser. After the fluid flows into the second-stage impeller and before it flows into the first-stage impeller (P8–P11), the main frequencies of pressure pulsation are distributed at 3fn (6 times), 5fn (2 times) and 10fn (1 time), the second-order frequencies are distributed at 3fn (2 times), 5fn (3 times), 6fn (1 time), 9fn (1 time) and 10fn (1 time), the third-order frequencies are distributed at 5fn (2 times), 6fn (1 time), 10fn (3 times), 15fn (2 times) and 20fn (1 time), and the third frequency is distributed at 0.5fn (2 times), fn (1 time), 6fn (1 time), 9fn (2 times), 10fn (1 time), 12fn (1 time), 15fn (1 time), and 20fn (1 time). 15fn represents the presence of dynamic and static interference between the primary and secondary impellers. It can be seen that in the fluid domain of the first-stage diffuser, the interstage interference frequency n*15fn between the two-stage impellers only occurs 2 times and 1 time in the statistics of the third-order frequency and the fourth-order frequency, respectively. Therefore, the interstage interference between the two-stage impellers is relatively small in this flow domain. When the fluid flows out of both impellers into the draft tube (P1–P7), the main frequency of pressure pulsation is distributed at 5fn (4 times), 6fn (8 times), the second-order frequency is distributed at 5fn (8 times) and 10fn (4 times), the third-order frequency

is distributed at 0.5fn (2 times), 1.5fn (1 time), 3fn (5 times) and 12fn (4 times), and the fourth-order frequency is distributed at 0.5fn (4 times), 3fn (1 time), 10fn (3 times), and 20fn (4 times). 5fn and its harmonics represent the propagation of pressure pulsation generated by the first-stage impeller to the draft tube. It can be seen that when the fluid flows out of the two impellers, in the low-flow condition, the blade frequency of the second-stage impeller that is farther away is the dominant frequency, and in the large-flow condition, the blade passing frequency of the first-stage impeller that is closer is the dominant frequency. The interstage interference frequency n*15fn between the two-stage impellers does not appear in the spectrum, so the interstage interference between the two-stage impellers will not cause pressure pulsation in the draft tube. Under large-flow conditions, more low-frequency signals with a frequency of 0.5fn are captured in the draft tube. The low-frequency signals in the draft tube are mainly generated by the vortex band. Combined with Figure 23, the amplitude of pressure pulsation generated by this frequency is as high as 40 kPa. The energy attenuation of low-frequency pulsation is very slow and can even spread throughout the pipeline, so it is necessary to add a suitable diversion device in the draft tube to eliminate the vortex band.

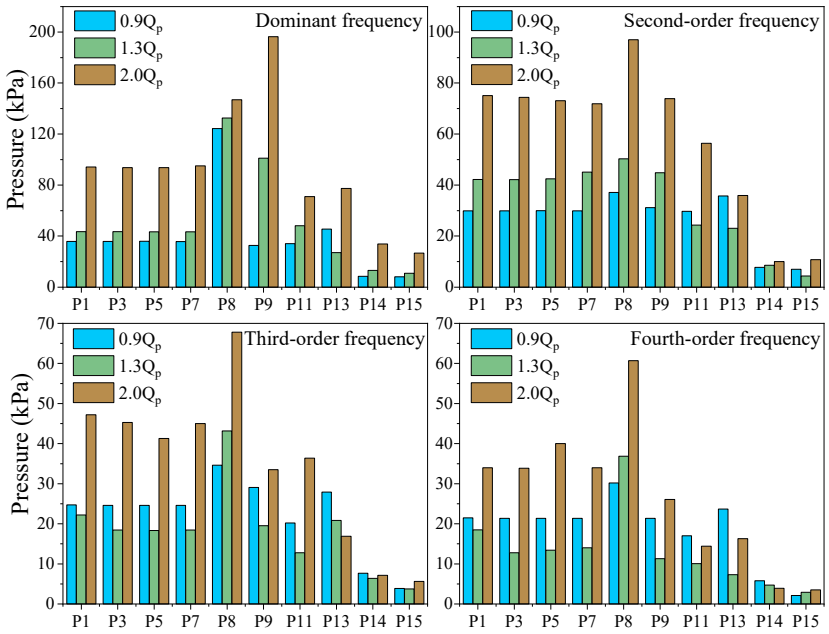

Figure 23. Amplitude distribution at the main frequency, second-order, third-order and fourth-order frequency.

4. Conclusions

Based on the CFD simulations, the internal flow mechanism and pressure pulsation characteristics of a two-stage PPAT in turbine mode are studied. The PPAT has a wider flow operating range, and the pressure pulsation interference effect among the two-stage impellers and the propagation relationship of pressure pulsation under multiple turbine conditions is analyzed, which is helpful for understanding the operating state of the PPAT and providing a theoretical basis for the optimal design and operation of the PPAT.

1. There is a high-pressure area near the blade inlet of the first-stage impeller; the pressure distribution in the diffusion section of the first-stage diffuser shows the asymmetry. The high and low pressures are distributed separately on both sides of the diffuser tongue, and this phenomenon is more obvious with the increase in flow. There are high- and low-pressure areas on both sides of the vortex tongue of the draft tube caused by the flow around the cylinder occurring on one side of the central circle under the low-flow condition. With the increase in flow, the high- and low-pressure distribution on both sides of the vortex tongue gradually disappears.

2. In the second-stage fluid domain (inflow runner), the large vortex fills the entire flow channel of the impeller under the low-flow conditions. As the flow increases, the large vortex in the impeller channel mainly appears in the trailing edge of the blade and its wake region near the suction surface of the blade, which is mainly caused by the flow separation. The distribution area of high-intensity vortex on the second-stage section is larger when the operating condition deviates from the optimal condition, and the scale of some vortices almost blocks half of the area of a single channel. With the increase in the flow, the vortex band in the draft tube is generated, and this phenomenon will have a direct impact on the outer wall of the draft tube, which will cause strong noise and pressure pulsation.
3. The interstage interference frequency n*15fn between the two-stage impellers also produces a strong pressure pulsation in the inflow runner. In the fluid domain between the two impellers, the main factor affecting the pressure pulsation is the rotor–stator interference effect, and the interstage interference between the two impellers is small. The interstage interference between the two-stage impellers will not cause pressure pulsation in the draft tube, and more low-frequency signals with a frequency of 0.5fn are captured in the draft tube under large-flow conditions, which are mainly generated by the vortex band.

Future research on multi-stage pump as turbines may focus on transient operating conditions and inter-stage interference.

Author Contributions: Writing—original draft preparation, Y.L.; Writing-review and editing, W.L.; methodology and software, Z.L. and Z.Z.; validation, X.L.; project administration, A.P.; funding acquisition, A.P. All authors have read and agreed to the published version of the manuscript.

Funding: This study was supported by Joint Funds of the National Natural Science Foundation of China (U20A20292); Natural Science Foundation of Jiangsu Province (BK20210771). Alexandre Presas would like to acknowledge the Serra Hunter Programme. Alexandre Presas and Yonggang Lu would like to acknowledge the PID2022-139479OB-C21 project founded by the AEI of SPAIN.

Data Availability Statement: Data are contained within the article.

Conflicts of Interest: The authors declare no conflicts of interest.

References

1. Chen, L.; Feng, H.; Ge, Y. Maximum Energy Output Chemical Pump Configuration with an Infinite-Low- and a Finite-High-Chemical Potential Mass Reservoirs. *Energy Convers. Manag.* **2020**, *223*, 113261. [CrossRef]
2. Hang, X. Study on the Influence of Blade Outlet Angle on Flow and Structural Dynamic Characteristics for Chemical Process Pumps. Master's Thesis, Jiangsu University, Zhenjiang, China, 2018.
3. Nejadali, J. Analysis and Evaluation of the Performance and Utilization of Regenerative Flow Pump as Turbine (PAT) in Pico-Hydropower Plants. *Energy Sustain. Dev.* **2021**, *64*, 103–117. [CrossRef]
4. Tang, X.; Jiang, W.; Li, Q.; Hou, G.; Zhang, N.; Wang, Y.; Chen, D. Analysis of Hydraulic Loss of the Centrifugal Pump as Turbine Based on Internal Flow Feature and Entropy Generation Theory. *Sustain. Energy Technol. Assess.* **2022**, *52*, 102070. [CrossRef]
5. Li, Y.; Zhang, L.; Zhang, Z.; Chen, D. Influence of blade wrap angle on performance in T-mode multistagehydraulic turbine. *J. Drain. Lrrigation Mach. Eng.* **2021**, *39*, 757–763.
6. Wang, T.; Liu, Y.; Dong, Y.; Xiang, R.; Bai, Y. The Influence of the Middle Bending Shape of the Blade on the Performance of a Pump as Turbine. *Energy* **2024**, *295*, 131000. [CrossRef]
7. Lei, S.; Cheng, L.; Yang, W.; Xu, W.; Yu, L.; Luo, C.; Jiao, W.; Shen, J. Dynamic Multiscale Pressure Fluctuation Features Extraction of Mixed-Flow Pump as Turbine (PAT) and Flow State Recognition of the Outlet Passage Using Variational Mode Decomposition and Refined Composite Variable-Step Multiscale Multimapping Dispersion Entropy. *Energy* **2024**, *305*, 132230. [CrossRef]
8. Tchada, A.M.; Tchoumboué, N.; Mesquita, A.L.A.; Hendrick, P. Enhancing Pump as Turbine (PAT) Performances: A Numerical Investigation into the Impact of Impeller Leading Edge Rounding. *Heliyon* **2024**, *10*, e34663. [CrossRef]
9. Chen, X.; Zhang, Z.; Huang, J.; Zhou, X.; Zhu, Z. Numerical Investigation on Energy Change Field in a Centrifugal Pump as Turbine under Different Flow Rates. *Renew. Energy* **2024**, *230*, 120804. [CrossRef]
10. Yang, F.; Xu, G.; Guo, J.; Li, Z.; Luan, Y.; Tang, F. Transient Dynamic Stress Behavior Analysis of the Axial Flow Pump as Turbine at Part Loads. *Alex. Eng. J.* **2024**, *99*, 180–195. [CrossRef]
11. Zhu, Z.; Gu, Q.; Chen, H.; Ma, Z.; Cao, B. Investigation and Optimization into Flow Dynamics for an Axial Flow Pump as Turbine (PAT) with Ultra-Low Water Head. *Energy Convers. Manag.* **2024**, *314*, 118684. [CrossRef]

12. Nguyen, D.-A.; Kim, J.-H. Co-Adjustable Guide Vane and Diffuser Vane to Improve the Energy Generation Potential of an Axial-Flow Pump as Turbine. *Energy* **2024**, *291*, 130325. [CrossRef]
13. Renzi, M.; Nigro, A.; Rossi, M. A Methodology to Forecast the Main Non-Dimensional Performance Parameters of Pumps-as-Turbines (PaTs) Operating at Best Efficiency Point (BEP). *Renew. Energy* **2020**, *160*, 16–25. [CrossRef]
14. Derakhshan, S.; Nourbakhsh, A. Experimental Study of Characteristic Curves of Centrifugal Pumps Working as Turbines in Different Specific Speeds. *Exp. Therm. Fluid Sci.* **2008**, *32*, 800–807. [CrossRef]
15. Zhang, J.; Appiah, D.; Zhang, F.; Yuan, S.; Gu, Y.; Asomani, S.N. Experimental and Numerical Investigations on Pressure Pulsation in a Pump Mode Operation of a Pump as Turbine. *Energy Sci. Eng.* **2019**, *7*, 1264–1279. [CrossRef]
16. Feng, J. *Numerical and Experimental Investigations on Rotor-Stator Interaction in Radial Diffuser Pumps*; Shaker Verlag GmbH: Düren, Germany, 2009.
17. Wang, C.; Shi, W.; Wang, X.; Jiang, X.; Yang, Y.; Li, W.; Zhou, L. Optimal Design of Multistage Centrifugal Pump Based on the Combined Energy Loss Model and Computational Fluid Dynamics. *Appl. Energy* **2017**, *187*, 10–26. [CrossRef]
18. Yang, S.-S.; Kong, F.-Y.; Qu, X.-Y.; Jiang, W.-M. Influence of Blade Number on the Performance and Pressure Pulsations in a Pump Used as a Turbine. *J. Fluids Eng.* **2012**, *134*, 124503. [CrossRef]
19. Yang, S.-S.; Liu, H.-L.; Kong, F.-Y.; Xia, B.; Tan, L.-W. Effects of the Radial Gap Between Impeller Tips and Volute Tongue Influencing the Performance and Pressure Pulsations of Pump as Turbine. *J. Fluids Eng.* **2014**, *136*, 054501. [CrossRef]
20. He, Y. Variation Law of External Characteristics of Mixed-flow Pump as Hydraulic Turbine at Different Wrapping Angles. *Yunnan Water Power* **2022**, *38*, 199–202.
21. Bi, Z.; Liang, Y.; Yi, Y.; Zhang, Y. Influence of Rotating Speed on the Performance of Hydraulic Turbine withGuide Vane. *J. Eng. Therm. Energy Power* **2021**, *36*, 46–53. [CrossRef]
22. Pugliese, F.; Fontana, N.; Marini, G.; Giugni, M. Experimental Assessment of the Impact of Number of Stages on Vertical Axis Multi-Stage Centrifugal PATs. *Renew. Energy* **2021**, *178*, 891–903. [CrossRef]
23. Gu, Y.; Bian, J.; Wang, Q.; Stephen, C.; Liu, B.; Cheng, L. Energy Performance and Pressure Fluctuation in Multi-Stage Centrifugal Pump with Floating Impellers under Various Axial Oscillation Frequencies. *Energy* **2024**, *307*, 132691. [CrossRef]
24. Zhao, J.; Pei, J.; Wang, W.; Gan, X. Blade Redesign Based on Inverse Design Method for Energy Performance Improvement and Hydro-Induced Vibration Suppression of a Multi-Stage Centrifugal Pump. *Energy* **2024**, *308*, 132862. [CrossRef]
25. Si, Q.; Xu, H.; Deng, F.; Xia, X.; Ma, W.; Guo, Y.; Wang, P. Study on Performance Improvement of Low Specific Speed Multistage Pumps by Applying Full Channel Hydraulic Optimization. *J. Energy Storage* **2024**, *99*, 113238. [CrossRef]
26. Li, X.; Lu, Y.; Shi, W.; An, C.; Zhang, Z.; Zhao, Y. Study on Energy Conversion Characteristics and Pressure Fluctuation Interference Characteristics between Two Stage Impellers of the Pump as Turbine. *Proc. Inst. Mech. Eng. Part A J. Power Energy* **2023**, *237*, 718–728. [CrossRef]
27. Yan, X.; Zhang, F.; Zheng, Y.; Kan, K.; Rossi, M. Numerical Investigation of Hydraulic Instability of Pump-Turbines in Fast Pump-to-Turbine Transition. *J. Energy Storage* **2024**, *96*, 112731. [CrossRef]
28. Ping, X.; Yang, F.; Zhang, H.; Zhang, J.; Zhang, W.; Song, G. Introducing Machine Learning and Hybrid Algorithm for Prediction and Optimization of Multistage Centrifugal Pump in an ORC System. *Energy* **2021**, *222*, 120007. [CrossRef]
29. Tan, M.; Lian, Y.; Wu, X.; Liu, H. Tests for Effects of Impeller Timing on Vibration Characteristics of a Multi-Stage Centrifugal Pump. *J. Vib. Shock* **2020**, *39*, 1–7.
30. Maleki, A.; Ghorani, M.M.; Haghighi, M.H.S.; Riasi, A. Numerical Study on the Effect of Viscosity on a Multistage Pump Running in Reverse Mode. *Renew. Energy* **2020**, *150*, 234–254. [CrossRef]
31. Dimas, A.A.; Vouros, A.P. Effect of Cross-Flow Velocity at Forebay on Swirl in Pump Suction Pipe: Hydraulic Model of Seawater Intake at Aliveri Power Plant in Greece. *J. Hydraul. Eng.* **2012**, *138*, 812–816. [CrossRef]
32. Song, X.; Yao, R.; Chao, L.; Wang, Z. Study of the Formation and Dynamic Characteristics of the Vortex in the Pump Sump by CFD and Experiment. *J. Hydrodyn.* **2021**, *33*, 1202–1215. [CrossRef]
33. Song, X.; Chao, L.; Wang, Z. Prediction on the Pressure Pulsation Induced by the Free Surface Vortex Based on Experimental Investigation and Biot-Savart Law. *Ocean. Eng.* **2022**, *250*, 110934. [CrossRef]
34. Song, X.; Luo, Y.; Wang, Z. Numerical Prediction of the Influence of Free Surface Vortex Air-Entrainment on Pump Unit Performance. *Ocean. Eng.* **2022**, *256*, 111503. [CrossRef]
35. Zeng, Y.; Yao, Z.; Wang, F.; Xiao, R.; He, C. Experimental and Numerical Investigations of Vibration Characteristics Induced by Pressure Fluctuations in a Parallel Operating Pumping System. *J. Hydraul. Eng.* **2021**, *147*, 04021020. [CrossRef]
36. Simpson, A.R.; Marchi, A. Evaluating the Approximation of the Affinity Laws and Improving the Efficiency Estimate for Variable Speed Pumps. *J. Hydraul. Eng.* **2013**, *139*, 1314–1317. [CrossRef]